Journal of Materials Chemistry C

ROYAL SOCIETY OF CHEMISTRY

PAPER

View Article Online
View Journal



Cite this: DOI: 10.1039/d5tc03143e

# Local structure of hydrated and dehydrated Prussian white cathode materials

Ida Nielsen, *[a] Maksim Eremenko,[bcd] Yuanpeng Zhang,[b] Matthew G. Tucker[b] and William R. Brant *[a]

The sodium iron hexacyanoferrate compound with chemical formula $Na_{2.04(2)}Fe[Fe(CN)_6]\cdot 2.24(2)H_2O$, also known as Prussian white (PW), contains disordered and dynamic water molecules that have a dualistic effect on its battery performance. Furthermore, the material exhibits severe strain when dehydrated, which over time diminishes the performance. To understand the complex role of water on the sodium ion conduction and the structural changes happening upon dehydration, local structural characterization is needed. Here, we report the first neutron total scattering study of PW. Reverse Monte Carlo (RMC) fitting reveals that local octahedral distortion of the nitrogen-bound iron octahedra contributes to the disorder of the framework. The strain observed in the dehydrated material comes from a combination of the Fe–N bond elongation and a disordered distribution of sodium throughout the larger structure. In the hydrated material, the sodium exhibits more order due to the presence of water, which constrains the sodium movement. However, the sodium ordering affects the orientation of the water molecules. In the low temperature $P2_1/n$ phase, sodium orders into planes with the oxygen atoms in the water molecules being in the plane, while the hydrogen atoms are pointing away from the sodium plane. In the room temperature $R\bar{3}$ phase, the sodium and water are less ordered despite similar frameworks. Sodium can take a wide range of positions, especially if no water molecule blocks its way, to obtain optimal bonding conditions. These results show that the relationship between sodium and water is co-dependent, and demonstrate that the local structure of framework materials has a crucial link to their properties.

Received 20th August 2025,
Accepted 1st December 2025

DOI: 10.1039/d5tc03143e

rsc.li/materials-c



## I. Introduction

The iron- and sodium-based Prussian blue analogue (PBA), $Na_2Fe[Fe(CN)_6]\cdot zH_2O$, also known as Prussian white (PW), is an attractive cathode material for sodium-ion batteries. The structure of PBAs consists of a porous framework with octahedrally coordinated transition metal centers that are linked by cyanide bridges. Alkali cations, such as sodium, and/or neutral guest species, such as water, can occupy the interstitial sites within the porous framework. The sodium-based PBAs adopt different structures depending on the sodium and water content.[1,2] This involves many phase transitions and large changes in the volume that are detrimental to the material's performance. Water contributes to stabilizing the structure,[3] thereby reducing the large volume changes. However, the presence of water also negatively affects the material's performance.[4,5] Thus, water must be replaced with another small molecule to enhance PBAs' performance in sodium-ion batteries. To achieve this, a better understanding of the mechanism behind the observed phase transitions is crucial to allow for the design of chemically modified PBAs.

A recent neutron diffraction study showed that hydrated PW exhibits a near room temperature phase transition from $P2_1/n$ to $R\bar{3}$ symmetry, which is due to an octahedral tilt transition.[1] In the $P2_1/n$ model obtained from the average structure, the water was distributed over two sites with partial occupancy, forming a plane with sodium occupying the interstitial sites. In addition, one of the oxygen atoms was included as a split site, indicating short-range disorder. When transforming to the $R\bar{3}$ phase, it was found that many different models with different distributions of the water could fit the data. Thus, it was not possible to determine the ordering of the water in this phase. Upon removal of crystal water, the $R\bar{3}$ symmetry was maintained, but the magnitude of the octahedral tilts increased significantly, resulting in structural collapse and peak broadening. The oxygen split site in the $P2_1/n$ phase and the loss of

[a] Department of Chemistry – Ångström Laboratory, Uppsala University, Box 538, SE-751 21 Uppsala, Sweden. E-mail: ida.nielsen@kemi.uu.se, william.brant@kemi.uu.se
[b] Neutron Science Division, Oak Ridge National Laboratory, Oak Ridge, TN 37831, USA
[c] Materials Measurement Science Division, National Institute of Standards and Technology, Gaithersburg, MD 20899, USA
[d] Theiss Research, La Jolla, CA 92037, USA

the ordering of water when transitioning to the $R\bar{3}$ phase of hydrated PW together with the peak broadening observed in the diffraction pattern of dehydrated PW propose a need for local insight into the structure of hydrated and dehydrated PW.

A way of obtaining local information from a structure is total scattering with pair distribution function (PDF) analysis. Here, both the Bragg and diffuse scattering are considered allowing for an understanding of both the long- and short-range order in a material.[6] For PBAs, the use of neutron scattering is essential for obtaining accurate information about the position and occupation of sodium and water as well as the position of carbon and nitrogen that are connected to the octahedral tilting.[7] Therefore, neutron total scattering with PDF analysis provides a way of investigating the long- and short-range structure of PW. In addition, to understand the macroscopic properties of PBAs in batteries, such as the rapid onset of non-equilibrium phase transitions[8,9] and sodium diffusion, fundamental atomic origins, such as the local position of sodium and water and its influence on the PBA framework, are needed.

Here, we present a Reverse Monte Carlo (RMC) study of the local structure of hydrated and dehydrated PW. The dehydrated material consists of distortions of the nitrogen-bound iron octahedra and has a disordered distribution of sodium, which combined contributes to the observed strain. In the hydrated material, distortions of the nitrogen-bound iron octahedra are also present. Additionally, the ordering of the sodium dictates the orientational (dis)order of the water molecules, and sodium can take a wide range of positions within the PBA framework if no water molecules hinder its movement. By shedding light on the local structure and the interplay between sodium and water in PW, new materials optimized for battery applications can be developed.

# II. Methods

## A. Synthesis

Synthesis of the PW sample was done using an acid-decomposition approach. A solution of 0.44 M $Na_4[Fe(CN)_6]\cdot 10H_2O$ (Sisco Research Laboratories Pvt. Ltd; extra pure AR, 99%) in deionized and deoxygenated water was prepared and heated to 80 °C. A two-fold molar excess of HCl (37%) was added over 12 hours using a syringe pump to produce the acid-facilitated self-decomposition of $Na_4[Fe(CN)_6]\cdot 10H_2O$. The process lasted 24 hours with $N_2$ flowing at all times. The resulting precipitate was filtered under an inert atmosphere, washed four times with deionized and deoxygenated water, and dried under flowing $N_2$ in the filtration setup for 12–24 hours. Part of the sample was dehydrated at 190 °C for 48 hours under a $5.7 \times 10^{-3}$ mbar vacuum to produce the dehydrated PW sample. The resulting powders were stored in an argon-containing glovebox for further analysis.

## B. Sample characterization

The sodium and iron contents were determined from inductively coupled plasma-optical emission spectroscopy (ICP-OES) while the carbon, nitrogen, and hydrogen contents were determined from elemental analysis. The measurements were performed by Medac Ltd, United Kingdom. The water content was determined by thermogravimetric analysis (TGA) on a TA Instruments Q500. Approximately 5 mg of the sample was loaded onto an aluminium pan in the air before placing the sample into the TGA furnace under flowing $N_2$ (60 mL $min^{-1}$). The sample was heated from room temperature to 500 °C with a heating rate of 5 °C $min^{-1}$. The $[Fe(CN)_6]^{4-}$ vacancy content and the sodium content were determined by Mössbauer spectroscopy. The measurements were performed at room temperature using a constant acceleration type of vibrator and a $^{57}$CoRh source. The sample was enclosed in a sealed aluminium cover to form an absorber with a sample concentration of ~9 mg. The absorber was prepared inside an argon-containing glovebox. A calibration spectrum was recorded at 295 K using natural iron metal foil as a reference absorber. The spectra were folded and fitted using the least-square Mössbauer fitting program Recoil to obtain the values of the center shift (CS), the magnitude of the electric quadrupole splitting |QS|, the full-width at half-maxima ($W$) of the Lorentzian absorption lines, and the spectral areas ($A$). In-house X-ray diffraction (XRD) was performed on a Bruker D8 Powder diffractometer (double Cu Kα radiation $\lambda_1$ = 1.540600 Å and $\lambda_2$ = 1.5444390 Å) with a Lynxeye XE-T position sensitive detector. The sample was placed on a powder holder surrounded by a silicon disk. The experiments were performed between 10 and 80° with a step size of 0.02°.

## C. Neutron total scattering

Neutron total scattering data were collected on the NOMAD instrument at the Spallation Neutron Source at the Oak Ridge National Laboratory.[10] The pristine and dehydrated samples were packed in 3 mm quartz capillaries inside an argon-containing glovebox. The data were measured at 100 and 300 K for 1 hour at each temperature. In addition, data were measured at 330 K for hydrated PW to probe the $R\bar{3}$ phase (the phase transition takes place at ~308 K). The scattering from the empty instrument and an empty capillary was also measured and subtracted to isolate the elastic coherent scattering from the samples. The data reduction was done using the autoNOM package written by J. Neuefeind. The relative contribution from the incoherent scattering due to the presence of hydrogen in the pristine sample was removed using a pseudo-Voigt function, where the widths of the Lorentzian and Gaussian contributions, the mixture ratio between the two, the scale, and the offset were refined using least-squares. The XRD and ND patterns were refined in Topas Academic V6.[11] Small-box modeling was done using PDFgui[12] while big-box modeling was done using RMCProfile.[13,14] The generated data files for each software follow the nomenclature from Keen.[15] The structures were visualized using CrystalMaker.[16] For each data set, 10 unique RMC configurations were generated and analyzed to minimize statistical noise.

# III. Results and discussion

## A. Sample characterization

The composition of the pristine PW sample was determined to be $Na_{2.04(2)}Fe[Fe(CN)_6]\cdot 2.24(2)H_2O$ from ICP-OES, TGA, and

 

Mössbauer analysis (Fig. S1, S2 and Tables S1, S2). The Mössbauer spectrum of the pristine PW sample was fitted with two doublets. The assignments of the Mössbauer patterns to different iron sites were done following previously established procedures.[17–19] The pattern with a negative CS is from low-spin iron coordinated to six carbon atoms (denoted $Fe_C$) and the pattern with a positive CS is from high-spin iron coordinated to six nitrogen atoms (denoted $Fe_N$). The obtained spectral areas of 49.15(61) : 50.85(53) verify a vacancy-free, sodium-rich material. ICP-OES showed a slightly higher Na : Fe ratio of 1.06(2), however, considering the error of the analysis, it agrees with the sodium content determined from Mössbauer spectroscopy. TGA analysis showed a weight loss of 11.38(1)% from room temperature to 250 °C giving a water content of $2.24(2)H_2O$ per formula unit. This weight loss consists of both surface absorbed and crystal water. The laboratory XRD pattern of the pristine PW sample showed a monoclinic $P2_1/n$ phase (Fig. S3), which is one of the two phases that exist near room temperature for high sodium, iron-based, vacancy-free PBAs.[1] The laboratory XRD pattern of the dehydrated PW sample showed a rhombohedral $R\bar{3}$ phase (Fig. S4) as expected for the dehydrated material.

## B. The average structure

The diffraction data were refined using the Rietveld method[20] using $P2_1/n$ symmetry for the data collected at 100 and 300 K and using $R\bar{3}$ symmetry for the data collected at 330 K for hydrated PW. This produced satisfactory fits (Fig. S5–S7) with reasonable refined parameters (Tables S3–S5) except for high atomic displacement parameters (ADPs) for oxygen in the two $P2_1/n$ models at 100 and 300 K. The high ADPs, which do not change significantly between 100 and 300 K (11.5(4) $Å^2$ to 14.7(3) $Å^2$), indicate positional disorder *i.e.*, dynamics of the water. Water dynamics have been observed down to 45 K for a sample with similar composition.[3] For the $P2_1/n$ models at 100 and 300 K, sodium occupies the interstitial site while a single fully occupied oxygen site (fixed to the TGA-determined water content) was found occupying two of the PBA window faces. This is in contrast to a previous study, where two sites with partial occupancy were determined to occupy four of the six window faces.[1] The model with the two oxygen sites from the previous study was also tested against the data in this study, but did not yield an acceptable fit. Having water on the window face results in clear sodium channels along the *a* direction. For the $R\bar{3}$ model at 330 K, sodium occupies the interstitial site while a single but partially occupied oxygen site (fixed to the TGA-determined water content) was found occupying three of the PBA window faces. In this model, there are no clear sodium channels in any direction. In a previous neutron diffraction study, it was found that the 313 K data (corresponding to the $R\bar{3}$ phase) could be fitted with several different models with different oxygen distributions, indicating disorder of the water in the $R\bar{3}$ phase.[1] The position of sodium and water (at the center and window face, respectively) for all three models is in agreement with the previous neutron diffraction study of hydrated PW.[1]

For dehydrated PW, the data at 100 and 300 K were refined using $R\bar{3}$ symmetry (Fig. S8, S9 and Tables S6, S7). The refined models agree with a previous neutron diffraction study with sodium displacing along the *c* direction while the iron octahedra rotate (Fig. S10). During dehydration, the volume reduces by 18% (Fig. S11) and the diffraction peaks broaden relative to the hydrated material indicating loss of crystallinity. The loss of crystallinity can be due to either increased strain in the material or a reduced crystallite size. The volume change of the hydrated and dehydrated material upon temperature change is less than 2% in the temperature range 100 to 300 K (Fig. S11).

## C. The neutron pair distribution functions

The neutron pair distribution functions for hydrated and dehydrated PW are shown in Fig. 1. For all the PDFs, the peaks below 5 Å are sharper relative to the peaks at higher *r* suggesting that a structural unit is present in the materials which arrange in a disordered way to form the larger structure. Subtle variations in the PDF can be seen as a function of temperature, especially at 100 K, where some features around 4–6 Å are more pronounced due to less thermal motion. Above 3.5 Å, the main differences between hydrated and dehydrated PW appear, *e.g.*, the peaks at 4.1 and 5 Å in the PDFs of dehydrated PW are not present in the PDFs of hydrated PW. The presence of water, specifically hydrogen, in hydrated PW also affects the intensities observed in the PDFs relative to dehydrated PW since hydrogen has a negative coherent scattering cross section resulting in negative pair correlations in the PDF of hydrated PW. This is especially noticeable around 5 Å in the PDFs (grey area in Fig. 1). The PDFs at 300 and 330 K for hydrated PW are visibly very similar, thus, the phase transition from $P2_1/n$ to $R\bar{3}$ is not directly observable from only looking at the PDFs. This indicates that there are very subtle differences between the structural framework and the sodium and water environments in the two phases. However, modeling is required to obtain accurate structural information from the PDFs.

## D. PDF analysis of dehydrated Prussian white

**1. Small-box modeling.** Small-box modeling using PDFgui (Fig. S12) confirmed the hypothesis that the short-range structure is different from the long-range structure. The first 5 Å can be fitted well (Fig. S12a and b), however, when extending this

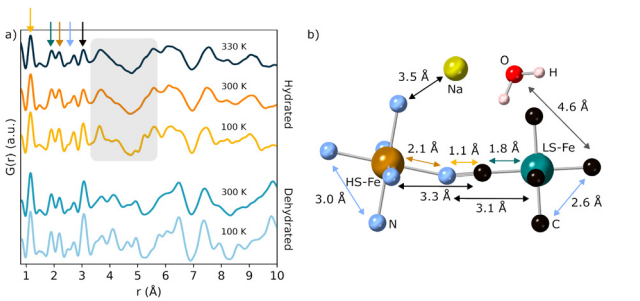


Fig. 1 (a) PDFs of hydrated and dehydrated PW from 100 to 330 K. The grey area highlights a region where the contribution from hydrogen is more pronounced. (b) Selected pair distances in the PDF.

model to fit a region up to 20 Å, there are large discrepancies (Fig. S12c and d). In general, most features in the PDF become very broad after 5 Å. By treating the peak width of the low $r$ and high $r$ regions separately, a reasonable fit can be obtained in the 1–20 Å range (Fig. S12e and f). However, features in the PDF at higher $r$ (*e.g.*, at 6, 8, 13, and 17 Å) are not fitted well by the model (especially at 100 K). Fitting only the 5–20 Å region (Fig. S12g and h) gives a reasonable fit with only minor features not described by the model. The first 5 Å corresponds to a structural unit consisting of eight iron octahedra connected by cyanide to form a PBA subcube (Fig. 3d) with a sodium ion occupying the available space within the subcube. The fact that the first 5 Å are very different from the long-range structure indicates that this structural unit might be connected to other similar units in a disordered way to make up the long-range structure. The connection between several of these subcubes will affect the rigidity of each octahedron to create the larger structure, and the sodium ions will also be distributed within the framework, creating additional disorder, which could lead to strain in the material. This hypothesis is indeed confirmed by the small-box modeling. Specifically, the difference between the model of the 1–5 Å region and the model of the 5–20 Å region is that in the 5–20 Å model, there is a broader distribution of bond angles and lengths within the iron octahedra and the sodium is more distributed throughout the structure. In contrast, the 1–5 Å model has a closer to ideal octahedral shape and a smaller distribution of sodium, suggesting that within each subcube, order is present. To model both the short- and long-range structures, big-box modeling was employed.

**2. Big-box modeling.** The big-box modeling was done using the RMC method, where the contents of a large supercell are moved around randomly until an agreement with the experimental data is achieved. This method does not rely on symmetry but several constraints, such as interatomic potentials and distance window constraints, can be applied to keep the structural framework together and obtain chemically plausible structures. In addition, the model can be guided by refining against different data containing different types of information about the system. The big-box modeling of the data for dehydrated PW was done using a supercell consisting of 12 960 atoms (a $9 \times 5 \times 3$ expansion of the unit cell) to simultaneously fit the $F(Q)$ and $G(r)$ data (Fig. 2a and Fig. S13). Due to the hexagonal cell from the $R\bar{3}$ symmetry (having a 120° angle), an orthorhombic cell (all angles being 90°) was derived from the hexagonal cell to avoid any hexagonal bias in the RMC fitting.[21] Interatomic potentials were applied to the Fe–C, Fe–N, and C–N bonds and angles to retain the octahedral shape during the refinement, and a minimum distance window to avoid non-physical distances (Tables S8–S12). Comparison of the fit to the $G(r)$ (Fig. 2a) using the average structure and the RMC refined structure shows that the average structure overall lacks disorder of both the iron octahedra and the sodium atoms. This disorder is achieved in the RMC refinements, where the crystal structure is maintained but local disorder of the atomic positions has been added (Fig. 2b).

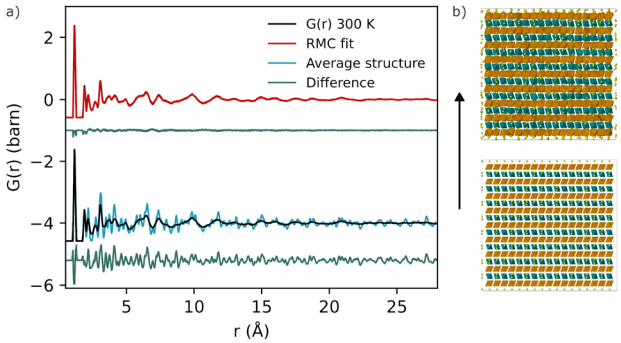


Fig. 2 RMC fits of the $G(r)$ and $F(Q)$ for dehydrated PW at 300 K showing the comparison between the fit to the PDF using the average structure (a 0.002 Å$^2$ displacement was added) and after RMC fitting. (b) Comparison of the PBA framework and sodium before (bottom) and after (top) RMC fitting. Similar was observed at 100 K.

**3. The PBA framework.** The PBA framework is analyzed through the partial radial distribution functions (RDF). The RDFs describe contributions from the different atom pairs that combined make up the total PDF. The Fe–Fe RDF measures the distortion of the framework (Fig. 3a). The RDF has a tight, Gaussian distribution around the average Fe–Fe distance, indicating minor displacements of the iron atoms. The first four peaks at 4.9, 6.5, 7.3, and 8.1 Å correspond to distances within a subcube (Fig. 3d), where the first peak is the length of a subcube. The RDF consists of sharp peaks also at higher distances, indicating that the framework orders throughout the larger structure and that the iron atoms do not move significantly. This observation agrees with how the PBA framework is built up, since the iron atoms are connected *via* the cyanide ligands, which have more degrees of freedom relative to the iron. The C–N, Fe–C, and Fe–N RDFs give a deeper insight into the disorder of the individual iron octahedra (Fig. 3b). The Fe–N bond is broader (2–2.5 Å) than the Fe–C bond (1.75–2.1 Å) due to the more ionic bond and generally weaker bonding character. The broadening becomes more significant at higher temperatures due to increased thermal motion. In addition, the Fe–N bond has an asymmetric distribution towards larger distances, while the Fe–C bond has a symmetric distribution, indicating bond elongation in the nitrogen-bound iron octahedra. With the higher degree of freedom of the cyanide ligands, the Fe–N bond needs to elongate to compensate for that movement, since the iron is displacing very little. The average Fe–N bond distance is 2.30 Å, while it is 1.94 Å for the Fe–C bond. The C–N bond is centered around 1.16 Å and does not change with temperature, which is reasonable to expect for a rigid triple bond.[22] The average C–Fe–C bond angle across the two temperatures is 90.0°, while it is 89.1° for the N–Fe–N bond angle. These are both close to the ideal octahedral angle of 90°. Since the bond angles are Gaussian distributed around 90° (Fig. S14a), the distortions of the iron octahedra come from bond elongation in the nitrogen-bound octahedra. This elongation disrupts the crystallinity, thereby contributing to the observed strain (*i.e.*, peak broadening) in the material.

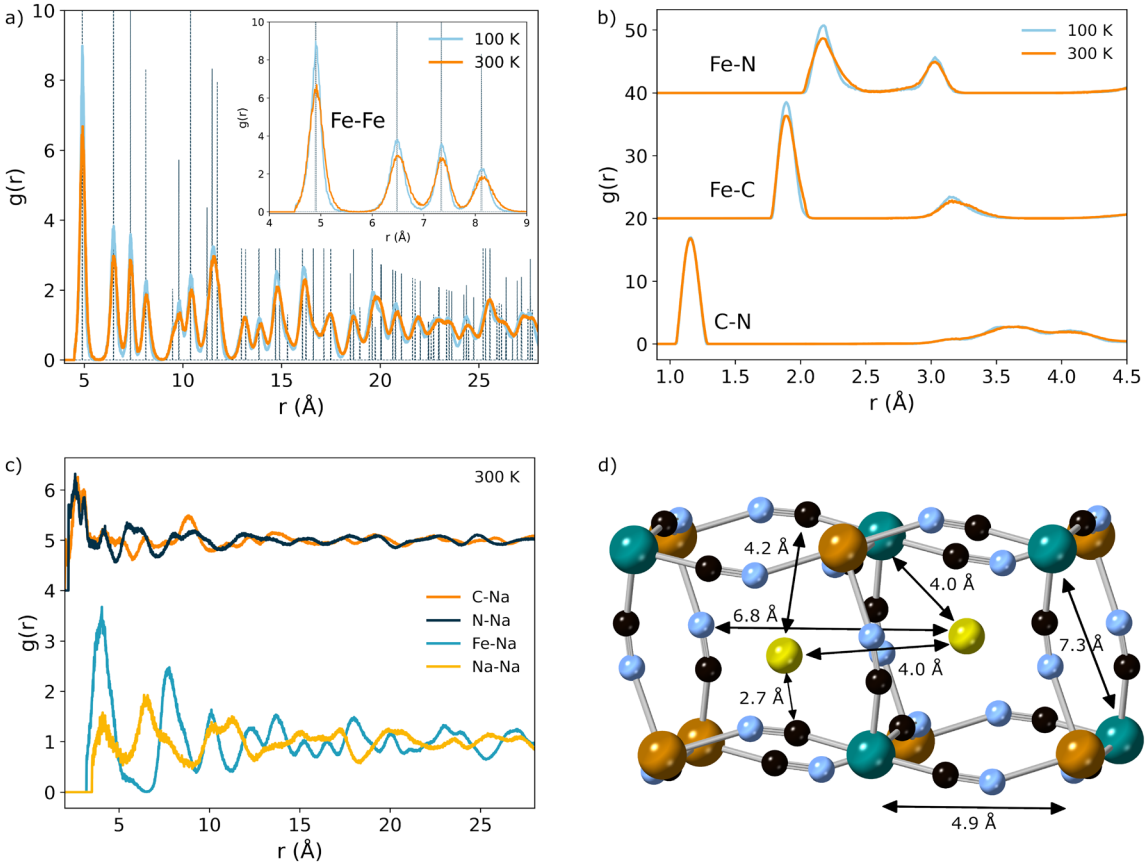


Fig. 3 (a) Fe–Fe RDFs at 100 and 300 K obtained from the RMC fitting. The dashed lines represent the average position. The inset shows a zoom of the first four RDF peaks. (b) C–N, Fe–C, and Fe–N RDFs at 100 and 300 K. (c) C/N/Fe/Na–Na RDFs at 300 K. The C/N–Na RDFs have been shifted by four along the *y* axis for visibility. Similar was observed at 100 K. (d) Two subcubes cut out of the RMC supercell showing selected distances.

A consequence of drying PW is an 18% reduction in the volume (Fig. S11). This is due to the tilting of the iron octahedra as the water is removed. The amount of tilting is defined by how much the Fe–C–N–Fe angles deviate from 180°. The Fe–N–C bond angle is more flexible due to the more ionic character and is also observed to bend more in the RMC models with a bond angle distributed around 145° (Fig. S14b). This angle distribution becomes broader and shifts towards higher angles with increasing temperature. On the other hand, the Fe–C–N bond angle is Gaussian distributed around 180°, maintaining linearity because of the more covalent Fe–C bond. This is in agreement with the average structure reported here and previously.[1]

**4. Sodium translation.** The deviation of sodium's average position relative to its position in the RMC model was calculated and assembled into histograms (Fig. 4a). Sodium is Gaussian distributed in two directions, but exhibits a broadening along *c* that increases with temperature due to increased thermal motion. The deviation along *c* is *ca.* ±2.5 Å (two and a half times compared to the two other directions), however, most of the sodium is within ±1 Å, *i.e.*, the atoms are mainly located around the average position but are smeared out from this position. This indicates that the sodium is more disordered than the framework, but is still limited to the space within each PBA subcube. PDF analysis cannot provide time resolution, but the observed average disorder of sodium agrees with PW's application as a sodium conductor, *i.e.*, the sodium is expected to move within the PBA framework.[23] The sodium translation along *c* is also evident from the condensed supercell (Fig. 4b).

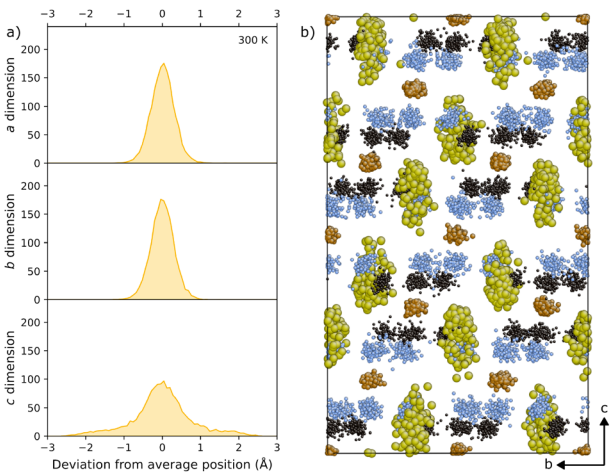


Fig. 4 (a) Histogram of the atomic deviations for sodium at 300 K in dehydrated PW. (b) Condensed supercell showing the distribution of the atoms. Similar was observed at 100 K.

The C/N–Na RDFs reveal the coordination environment for sodium (Fig. 3c). The RDFs are similar below 4.5 Å, which corresponds to distances within one subcube (Fig. 3d). Two peaks are present around 2.7 and 3.1 Å, showing the shift of sodium away from the subcube center and towards the cyanide ligands. The shift is towards one of the corners or the window faces of a subcube to achieve optimal bonding conditions between sodium and the cyanide ligands. Consequently, a shift in one direction gives the peak at *ca.* 4.2 Å for the cyanide ligands in the opposite direction of the shift. The peak around 2.7 Å is shifted to slightly lower distances for the N–Na RDF, indicating that sodium is positioned slightly closer to nitrogen than carbon due to the more concentrated electron density on nitrogen. After the first subcube, the two RDFs deviate, meaning that the correlation between sodium and carbon/nitrogen differs between subcubes throughout the medium- and long-range structure. The deviation is more severe between neighboring subcubes (5–10 Å) than at larger distances. This deviation stems from the more disordered nitrogen, as nitrogen is observed to stretch away from its associated iron. In addition, nitrogen can also move more freely due to the weaker bonding to iron, thereby resulting in different and broader correlations to sodium compared to carbon.

The Fe/Na–Na RDFs reveal the coordination environment for sodium relative to the framework and itself (Fig. 3c). The Fe–Na RDF has its first peak at 4 Å with a shoulder peak at 4.5 Å. The bimodal distribution for the Fe–Na partial further confirms the conclusions about the sodium shifting from the center of the subcubes towards off-center positions as seen from the C/N–Na RDFs. The Na–Na partial has its first peak at 4 Å, separating a sodium atom from another sodium atom in the surrounding subcubes. The sodium does not go closer to each other, mainly due to the minimum distances applied. The Na–Na partial is broader than the Fe–Na partial, illustrating the disorder of sodium throughout the structure. The disordered sodium contributes to the observed strain in the diffraction pattern.

Overall, dehydrated PW exhibits structural disorder of the nitrogen-bound iron octahedra and the sodium atoms. The iron atoms are static and locked into the PBA framework, while the distortions of the iron octahedra come from Fe–N bond length elongation. In contrast, the carbon-bound iron octahedra remain rigid due to the more covalent character. These results suggest that the tilting of the iron octahedra, which is used to describe the average structure,[1] might disappear if the Fe–N bonds elongate, since it breaks the tilt pattern. However, on a local scale (*e.g.*, individual subcubes), the tilting is retained but might vary at different places locally throughout the larger structure. The sodium is randomly distributed throughout the larger structure with a slight preference along a single direction. The disorder of the sodium in combination with the Fe–N bond length elongation contributes to the observed strain in the material.

### E. PDF analysis of hydrated Prussian white

The PDF analysis of the data from hydrated PW is more complex due to the presence of disordered water molecules containing hydrogen. Therefore, more careful steps in the analysis need to be taken.

**1. Starting configuration of the water molecules.** From the average structure, only the position of oxygen was determined. Therefore, the position and orientation of the hydrogen atoms in the water molecules are not known. Previous studies of the water dynamics in PW showed that water moves randomly within cavities suggesting that the orientation of the water molecules is random.[3] To get a representative description of the orientation of the water molecules in the big-box modeling, a starting configuration was prepared where the water molecules were allowed to move around randomly (Fig. S15). This starting configuration (one generated for each temperature) was then used in the RMC fitting.

**2. Modeling overlapping peaks in the PDF.** In the PDF of hydrated PW, the first negative peak corresponds to the O–H bond in a water molecule, the second peak corresponds to the C–N bond, and the third peak corresponds to the H–H bond. The initial RMC fitting of the PDF showed that there is an overlap between the O–H and C–N RDFs (Fig. 5a) which in the RMC fitting partly compensate for each other due to the negative scattering length of hydrogen. This resulted in water molecules with uneven O–H bonds and very short C–N distances, which consequently affected the iron octahedra, in the RMC model. This behavior happened despite the applied interatomic potentials and distance window constraints. Usually, this problem can be solved by adding extended X-ray absorption fine structure (EXAFS) data to the RMC refinement since EXAFS data contains information about only a few coordination shells while the PDF covers the nanoscale range.[24] In addition, EXAFS is element specific, *i.e.*, the technique focuses only on a certain absorber and its local environment at a time. However, EXAFS is not possible for the current material since hydrogen has a very low scattering length with X-rays, and thus, would not be visible in the EXAFS data. In addition to the overlapping peaks, the O–H and H–H peaks are also affected by termination ripples (stemming from the truncation due to a finite $Q$ range) and the very intense C–N peak, which affects the peak intensities of the O–H and H–H peaks as well. This means that not all the intensity of the O–H and H–H peaks comes from the sample.

To overcome these problems in the RMC fitting, peak fitting of the $G(r)$ in the 0–1.7 Å range using Gaussian functions was applied. In this approach, an RMC fit to the $G(r)$ and $F(Q)$ data using a supercell with the appropriate composition of the material was performed with the interatomic potentials and distance window as the only constraints. From the resulting fit, the area of the O–H and C–N RDFs was determined by integration. To calculate the area correctly, the RDFs were normalized using their Faber–Ziman coefficients (Equation 1).

$$g_{\mathrm{m}j(r)\mathrm{norm}} = ((g_{\mathrm{m}j}(r) - 1)\cdot FZ_{\mathrm{m}j}) - FZ_{\mathrm{total}} \quad (1)$$

where $FZ_{\mathrm{total}}$ is the sum of the Faber–Ziman coeffients of the remaining $g_{\mathrm{m}j}(r)$ RDFs. Subtraction of 1 is done to account for the definition of the PDF (see eqn (10) in ref. 15). With the areas of the two RDFs determined, a fit to the O–H and C–N peaks in

 

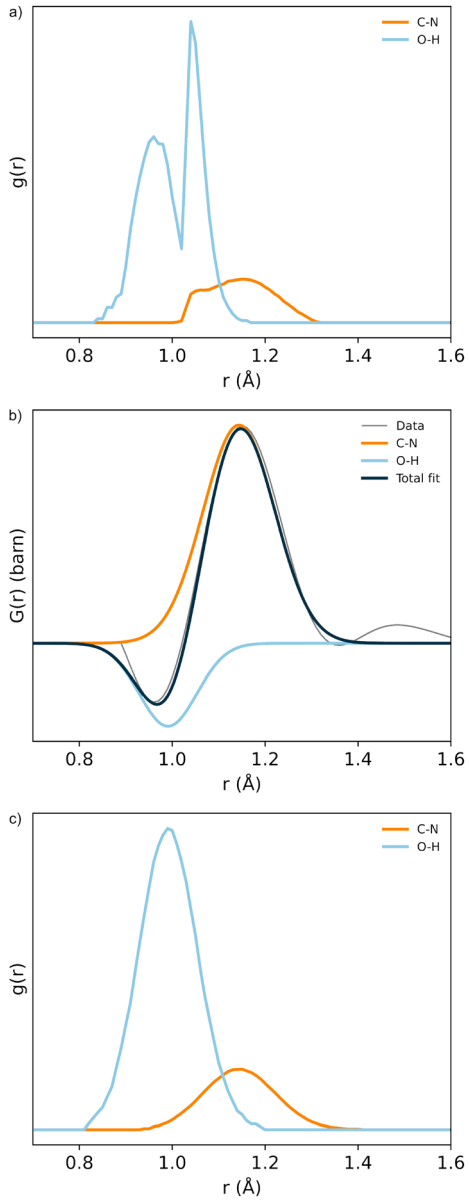


Fig. 5 (a) O–H and C–N RDFs using only interatomic potentials and distance window constraints. (b) Peak fitting of the $G(r)$ using Gaussian functions. (c) O–H and C–N RDFs after implementing the new data from the peak fitting.

the PDF using Gaussian functions could be made. The determined area was fixed while the peak positions and widths were allowed to vary. In this way, the model provides a more physically meaningful fit to the experimental PDF peaks (Fig. 5b), where the intensity from the sample and the intensity from other effects in the PDF are separated. The information about the peak positions from this fit was included in the interatomic potentials while the fitted peaks for the O–H and C–N RDFs were added as data (the blue and orange curves in Fig. 5b) to the RMC fitting. Since the H–H peak intensity is related to that of the O–H peak, it was not necessary to do peak fitting of the H–H peak using Gaussian functions. By using this approach, a nice overlap between the two RDFs was obtained with chemically meaningful distances for the O–H and C–N bonds (Fig. 5c). This method is reproducible over various data sets and different unique RMC runs (Fig. S16 and S17).

**3. Big-box modeling.** The big-box modeling for hydrated PW was done using a supercell consisting of 6336 atoms (a 4 × 6 × 6 expansion of the unit cell) for the data collected at 100 and 300 K and a supercell consisting of 11 106 atoms (a 7 × 3 × 4 expansion of the unit cell) for the data collected at 330 K. For the data at 330 K, an orthorhombic unit cell was created from the hexagonal cell similar to as described for dehydrated PW. The $G(r)$, $F(Q)$, Bragg data, and peak fitting data for the O–H and C–N RDFs were fitted simultaneously until the refinement had converged (Fig. S18–S20). Interatomic potentials were applied to the Fe–C, Fe–N, C–N, and O–H bonds and angles to retain the shape of the iron octahedra and water molecules during the fitting. Additionally, a minimum distance window and tails constraints were used (Tables S8–S12). The data is challenging to model due to the presence of hydrogen, however, the corrections made to the data (applying the hydrogen correction and creating additional data from peak fitting) improve the quality and the detail that is possible to extract from the fitting. For all fits, the difference between the data and the RMC model is greatest below 2 Å, which is the region where most constraints were applied. It was not attempted to improve this low $r$ region due to the risk of overfitting. However, the difference curve at low $r$ reflects what intensity comes from the sample and what intensity comes from termination ripples, especially around the H–H peak. The refined RMC models at all investigated temperatures all contain disorder of the iron octahedra and the sodium relative to the average structure of the hydrated material (Fig. S21). Note that the water molecules were already randomly oriented in the starting configuration.

**4. The PBA framework.** The PBA framework is first evaluated by the Fe–Fe RDF (Fig. S22a). The RDF peak is Gaussian distributed around the average position indicating minor displacements of the framework, as also observed for the dehydrated material. The first four peaks correspond to distances within a subcube. Above 14 Å, the RDF becomes broader due to peak overlap and increased thermal motion. Looking at the individual iron octahedra, elongation of the Fe–N bond is observed (Fig. S22b). The Fe–N bond is elongated (2–2.6 Å) due to the ionic character of the bond. However, the elongation is less severe compared to the dehydrated material. The average Fe–N bond length is 2.19 Å, while it is 1.92 Å for the Fe–C bond. The C–N RDF is Gaussian distributed around 1.15 Å constrained by the peak fitting data and the rigidity of the triple bond.[22] The C–Fe–C bond angle is Gaussian distributed around 90°, suggesting that the carbon-bound iron octahedra retain rigidity (Fig. S23a). The N–Fe–N bond angle has three distinct angles, which come from the higher flexibility and elongation of the Fe–N bond, *i.e.*, if one N–Fe–N angle becomes smaller, then the angle opposite within the same octahedra has to become the same amount larger (Fig. S23b), resulting in the two shoulder peaks at *ca.* 80° and 100°. Thus, there is both bond length and bond angle disorder in the nitrogen-bound iron octahedra. The average C–Fe–C bond angle across the

investigated temperatures is 86.7° while it is 92.4° for the N–Fe–N angle. These are both close to the ideal octahedral angle of 90°. Compared to the dehydrated sample, the tilting of the framework is less when water is present, with both the Fe–N–C and Fe–C–N angles centered around 180° (Fig. S23c). The distribution is similar across temperatures but differs in the width, with the Fe–N–C angle being slightly wider due to the more flexible Fe–N–C angle.

5. **Sodium translation.** Sodium translations are also present in the hydrated material. The histogram of sodium's deviation from its average position shows that in the $P2_1/n$ phase (100 and 300 K), the sodium is ordered into the *bc* plane, as observed from the average structure, with a distribution of ±2 Å from its average position (Fig. 6a). In the $R\bar{3}$ phase at 330 K, the sodium has a uniform distribution around its average position with a small fraction of the sodium moving ±2 Å further away along *b* and *c* (Fig. 6b).

The C/N–Na RDFs show three peaks up to 5 Å, which corresponds to distances within one subcube (Fig. 7a and Fig. S24a). Two of the peaks are centered around 3.1 and 3.6 Å corresponding to sodium being positioned around the center of the PBA subcube (Fig. 7e). The third peak is centered around 2.7 Å corresponding to some sodium atoms being positioned near the window faces of a subcube. The minimum distances applied in the RMC fitting constrain sodium from going closer to the cyanide and were kept to avoid overfitting. There is a slight deviation between the C/N–Na distances when entering a neighboring subcube. The C–Na RDF has a bimodal distribution (peaks at 5.6 and 6.8 Å) while the N–Na RDF has a broad unimodal distribution centered at 6.2 Å. Thus, sodium appears to be closer to carbon, which does not move a lot compared to nitrogen, which has larger displacements, resulting in a broader (more disordered) distribution. Above 7.5 Å, the C/N–Na correlations become similar to form the larger structure (Fig. S24a). In general, the sodium seems to occupy mainly near the center of the subcube, with a distribution in the *bc* plane for the $P2_1/n$ phase (that can extend to the window faces of the subcube). This behavior is also reflected in the histograms (Fig. 6a). At 330 K, the sodium is less ordered but shows some specific pathways through the framework (Fig. 6b), which also involves the window faces where water is not present.

The Fe/Na–Na RDFs (Fig. 7b and Fig. S24b) both have the first peak at 5.25 Å and the second peak at 7.35 Å. The first two peaks in the Na–Na RDF correspond to distances between sodium in neighboring subcubes. The first Fe–Na peak corresponds to the distance between sodium (at the center) and iron (at the corners) within a subcube (Fig. 7e). The second peak

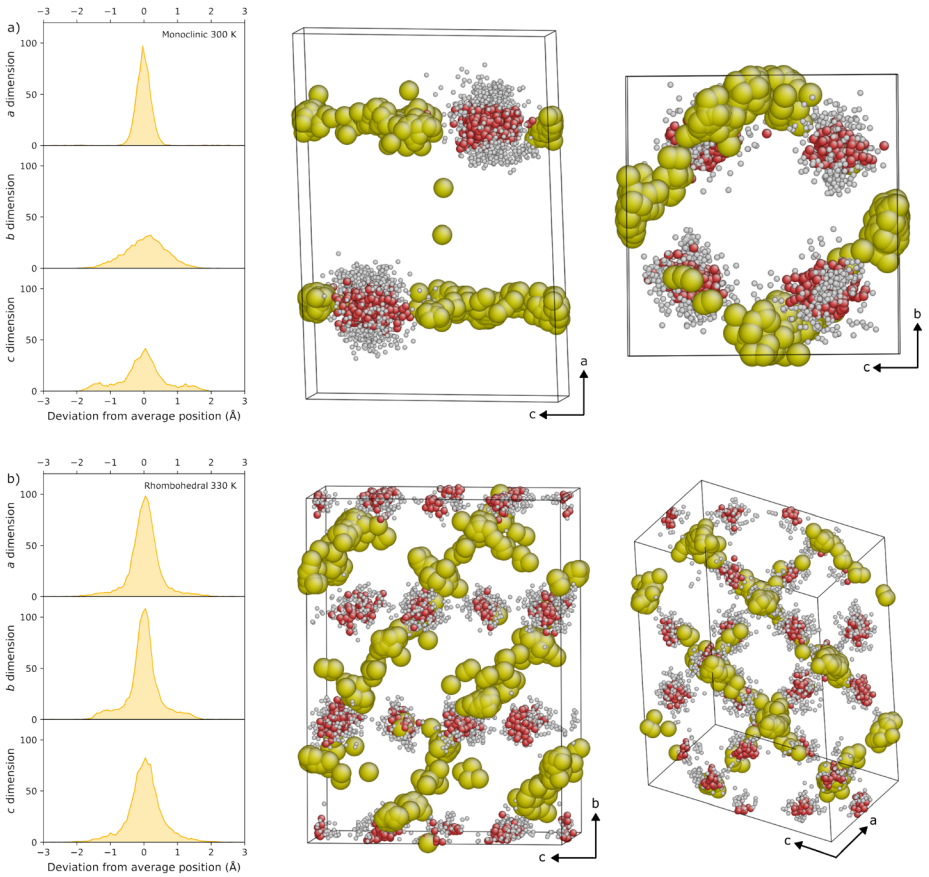


Fig. 6 (a) Histogram of the atomic deviations for sodium at 300 K with the condensed supercell emphasizing the layering of the sodium and the orientation of the water molecules. (b) Histogram of the atomic deviations for sodium at 330 K with the condensed supercell emphasizing the disordering of the sodium and the water molecules.

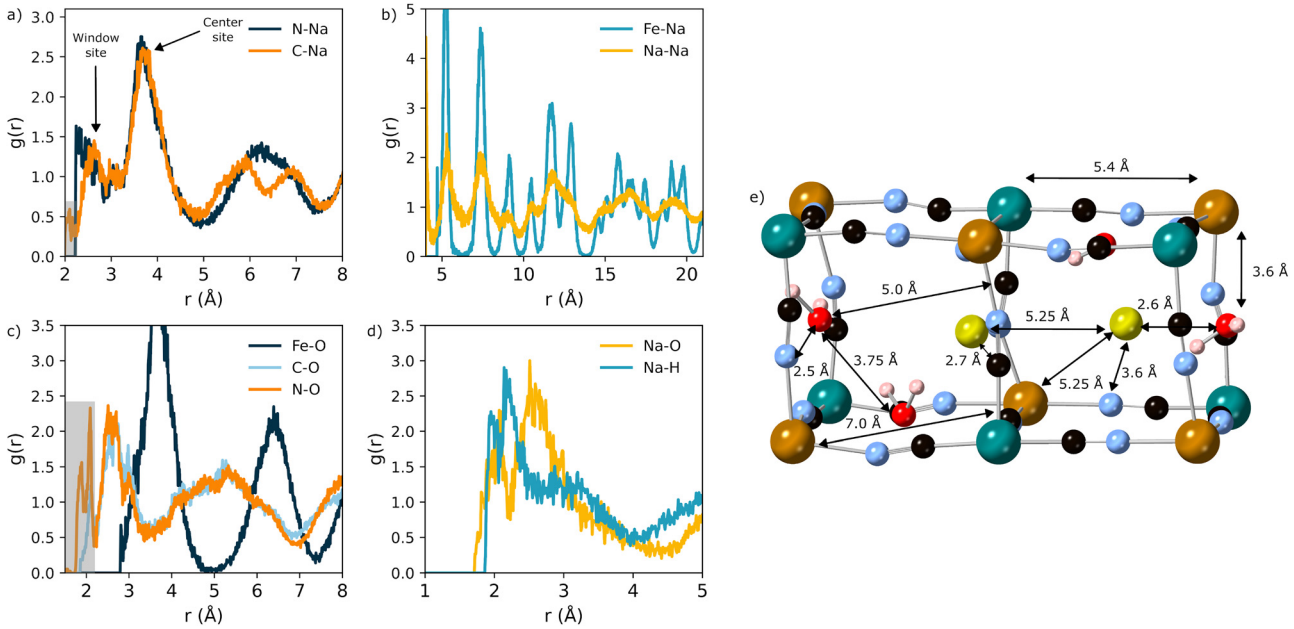


Fig. 7 RDFs for hydrated PW. (a) C/N–Na, (b) Fe/Na–Na, (c) Fe/C/N–O, and (d) Na–O/H. (e) Two subcubes cut out of the RMC supercell showing the different local environments present. All data is shown for 300 K with similar observations at 100 and 330 K. The peaks in the grey shaded area are fitting artifacts from the constraints applied in this region.

corresponds to the distance between sodium and iron atoms in neighboring subcubes. The Fe/Na–Na RDFs have similar correlations at all distances in $r$, but the Na–Na RDF is broader, indicating more disorder of the sodium, which is in line with the larger degrees of freedom that sodium has relative to iron, which is locked into the PBA framework. This is in contrast to the dehydrated material, where the Fe/Na–Na RDFs differed at longer distances (Fig. 3c). Thus, sodium is more ordered in the hydrated material relative to the dehydrated material, most likely due to the presence of water, which restricts sodium from moving in every direction.

**6. Water ordering.** The water coordination was evaluated by looking at the RDFs related to oxygen. The C/N–O nearest neighbor is 2.6 Å, which is the distance from the center of the window face to the cyanide ligands (Fig. 7c and Fig. S24c). Depending on the displacement of the water molecules away from the center, the distance can vary, giving the second peak at 3.0 Å. The broad distribution between 4–6 Å corresponds to the distance from a water molecule to cyanide ligands on adjacent and opposite window faces within a subcube (Fig. 7e). The intensity below 2.2 Å in the RDFs is attributed to artifacts in the fitting due to termination ripples and was constrained with minimum distances and tail constraints. The first Fe–O distance is at 3.7 Å. Again, this distance corresponds to having water at the center of a subcube window, and displacement away from this position gives the distribution around that distance. The second peak is at 6.3 Å, corresponding to the water relative to an iron atom in a neighboring subcube. The Fe–O RDF has sharper peaks than the C/N–O RDFs, meaning that this correlation is more ordered than the C/N–O correlations, suggesting that the movement of the cyanide ligands is more significant than the iron and water movement. This was also seen for the sodium-related RDFs (*e.g.*, C–Na *vs.* Fe–Na in Fig. 7a and b).

Since sodium orders into well-defined pathways (especially in the $P2_1/n$ phase), this might affect the orientation of the water molecules as well. Looking at the condensed supercell (Fig. 6a), it can be seen that in the $P2_1/n$ phase, where the sodium orders in the *bc* plane, the water adopts a sandwich orientation, *i.e.*, the oxygen is positioned in the same plane as sodium with the hydrogen atoms pointing away perpendicular to the sodium/oxygen plane. The negative dipole of the water molecule is thus surrounded by the positively charged sodium ions, while the positive dipole of the water points away from the sodium. This shows that there is orientational order of the water molecules in this phase. In the $R\bar{3}$ phase, the orientation of the water molecules is more random (Fig. 6b), possibly due to the more mobile sodium atoms and water molecules at this temperature. The nearest neighbor distance between sodium and water is evaluated by the Na–O partial (Fig. 7d and Fig. S24d). It is centered around 2.6 Å, which is the same distance found for the water cavities in the previous QENS study.[3] This suggests that the cavities observed with QENS are present in the structure, but the cavities can translate within the PBA framework depending on where sodium and water are locally. The cavities occupied by water are therefore not evenly distributed between two adjacent subcubes, as suggested from the average structure,[3] but can have different locations within the framework while maintaining the sodium–oxygen distance. In both phases, the coordination number was found to be 2.1 Na : O, meaning that every sodium atom has 2.1 water molecules surrounding it (and *vice versa*). This relationship is

seen to exist down to a sodium content of one sodium per formula unit,[25] after which the water content drastically decreases with decreasing sodium content. Thus, if one sodium disappears, there is still one sodium left for two water molecules, but after that, the water will leave the structure as well. The Na–H RDF (Fig. 7d and Fig. S24d) is centered around 2.2 Å with distributions up to 4 Å reflecting the different orientations the two hydrogen atoms in a water molecule can have relative to sodium. The Na–O/H RDFs have similar correlations at all distances, but the Na–H RDF is broader. The hydrogen atoms are more disordered relative to sodium because the two hydrogen atoms in a water molecule can have different orientations.

The water–water interactions were evaluated by the O–H, H–H, and O–O RDFs and the H–O–H angle. The average H–O–H angle in both phases is 104.2 with a Gaussian distribution, which is similar to the ideal bond angle of *ca.* 104.5° (Fig. S25a). The O–H bond distance is on average 1.01 Å with a Gaussian distribution constrained by the peak fitting data and interatomic potentials (Fig. S25b). The H–H bond distance is on average 1.59 Å with a slightly asymmetric distribution due to a wider distribution of H–O–H angles. The separation of the water molecules is measured by the O–O RDF. The first peak in the RDF is at 3.75 Å, corresponding to two water molecules on adjacent subcube window faces (Fig. S25b and c). The second peak is a bimodal distribution at 6.4 and 7.3 Å, corresponding to two water molecules in neighboring subcubes. The bimodal distribution is mainly observed in the $R\bar{3}$ phase, while the RDF peak more resembles one broad, asymmetric peak in the $P2_1/n$ phase. This is in line with the average structure, where the water is in the *bc* plane in the $P2_1/n$ phase (occupying two of the six window faces in one subcube) while in the $R\bar{3}$ phase, the water occupies three of the six window faces, thereby creating slightly different medium-range correlations of the water molecules in the two phases. At larger distances, the water–water interactions become similar for the two phases (Fig. S25b). The H–H RDF has similar features as the O–O RDF in the medium-range but is significantly broader at higher *r* due to the broader range of positions that the two hydrogen atoms in a water molecule can take.

Overall, the hydrated material exhibits bond length and bond angle disorder of the nitrogen-bound iron octahedra, while the carbon-bound iron octahedra are more rigid. Until now, experimental and theoretical studies have not agreed on the position of sodium and water within the PBA framework. Experimental studies based on neutron diffraction indicate that sodium occupies the center of the PBA subcube, while water is positioned on the window faces.[1,26] On the other hand, theoretical studies agree that the most favorable PBA structure has sodium positioned off-center or at the window faces, while water occupies the center of the subcube.[27–29] This discrepancy is due to different reasons. Firstly, smaller cations, such as lithium and sodium, are thought to occupy the window faces due to their smaller size and the possibility of obtaining optimal bonding conditions when surrounded by the cyanide ligands.[7,30] Larger cations, such as potassium, are too big to occupy the window faces and are therefore occupying the center of the subcube.[31,32] Secondly, the PBA framework is disordered and thus not a single stable configuration exists, but instead a fluctuating energy landscape, where the local environment changes with temperature. Thirdly, the functional used in the theoretical studies might also affect the results obtained. The RMC analysis in this work revealed a broader distribution of sodium positions, with sodium being able to both occupy the available space around the center of the PBA subcube and also being able to move closer to the window faces if no water molecule occupies the window. A similar phenomenon was observed in a recent inelastic neutron scattering study, which found that most of the sodium is located closer to the window faces with water occupying the center position, allowing it to move more freely.[3,33] Thus, the position of sodium proved more complex, with the presence of water dictating what positions sodium can take, *i.e.*, sodium can only move closer to the window faces if there is no water molecule present at this position. This shows that sodium-based PBAs are more dynamic than previously thought, and that it is hard to predict the sodium and water position using only size arguments, and from the average structure alone. Local probes, such as total scattering and inelastic neutron scattering,[33] are therefore essential for understanding these materials. Fitting of the Bragg data in the RMC fitting proved to affect the distribution of sodium significantly (see Section VII in the SI). The sodium ordering also affects the orientation of the water molecules. During the phase transition, the orientation of the water molecules becomes more disordered as the sodium distribution in the $R\bar{3}$ phase is less ordered relative to the $P2_1/n$ phase. At 330 K, both sodium and water are expected to be more mobile, which subsequently leads to more disorder in this phase. However, it is hard to say whether the sodium affects the water or the opposite. The sodium and water motions are most likely correlated, and this can affect the sodium ion conduction in the material.

## IV. Conclusions

Through neutron total scattering and RMC analysis, a fundamental understanding of the local structure in hydrated and dehydrated PW was obtained. Both the hydrated and dehydrated material exhibit octahedral distortions of the nitrogen-bound iron octahedra. The sodium is distributed throughout the dehydrated material with a preference for the *c* direction. The disordered sodium distribution and Fe–N bond elongation in the dehydrated material contribute to the strain observed in the Bragg data. Analysis of the data for hydrated PW revealed that the position of sodium is not fully apparent in the data for the average structure alone. Sodium can take a wide range of positions spanning the center of the subcube and out towards the window faces if no water molecule blocks its way. This is done in layers in the $P2_1/n$ phase, while the sodium ordering is less in the $R\bar{3}$ phase. The water obtains specific orientations in the $P2_1/n$ phase as a consequence of the sodium layering, with the hydrogen atoms pointing away from the sodium–oxygen

 

layer, while in the $R\bar{3}$ phase, the water molecules have less orientational order. These results show how the water and sodium ordering changes during phase transitions and that local octahedral distortions are an inherent property of these framework materials. The fact that sodium and water interact strongly and also determine preferred occupancy sites and diffusion pathways is the origin of the sluggish dehydration, and why high temperatures, vacuum pressure, and long dehydration times are needed to fully dehydrate the material.[34,35] The ability of the framework to distort and the inherent flexibility make it possible to retain structural integrity during extensive battery cycling.[8] A similar complex interplay between sodium and another guest molecule could exist, and the local structure of solvent-modified PBAs must be considered when designing new cathode materials.

## Author contributions

Ida Nielsen: conceptualization. Methodology. Validation. Formal analysis. Investigation. Data curation. Writing – original draft. Writing – review & editing. Visualization. Project administration. Maksim Eremenko: methodology. Formal analysis. Data curation. Writing – review & editing. Yuanpeng Zhang: software. Formal analysis. Data curation. Writing – review & editing. Matthew G. Tucker: resources. Data curation. Writing – review & editing. Supervision. William R. Brant: conceptualization. Validation. Resources. Writing – Review & editing. Supervision. Funding acquisition.

## Conflicts of interest

W. R. B. is a co-founder of the company Altris AB, which produces Prussian white powder for sodium-ion battery applications.

## Data availability

It includes the $S(Q)$ files for all five temperatures investigated. The PDFs can be derived from any PDF data preparation software. The hydrogen background has been removed from the $S(Q)$ for the samples containing hydrogen in the uploaded files.

The data supporting this article have been included as part of the supplementary information (SI). Supplementary information: the sample characterization, Rietveld refinements, small-box modeling, RMC fits, and details about the fitting procedure. A zip file containing the $S(Q)$ is also provided. See DOI: https://doi.org/10.1039/d5tc03143e.

## Acknowledgements

This research is funded by Stiftelsen för Strategisk Forskning (SSF) within the Swedish National Graduate School in Neutron Scattering, SwedNess (GSn15-0008). W. R. B. acknowledges funding from the Strategic Research Area StandUp for Energy and Energimyndigheten (45517-1). This research used resources at the Spallation Neutron Source, a DOE Office of Science User Facility operated by the Oak Ridge National Laboratory. The beamtime was allocated to NOMAD on proposal number IPTS-31723.1. The statistical RMC simulations were enabled by resources in project UPPMAX 2025-2-65 provided by Uppsala University at UPPMAX. Djurdjija Dzodan is acknowledged for performing the synthesis of the pristine sample, while Fredrik Lindgren is acknowledged for performing the Mössbauer experiment and analysis. Research conducted by M.E. was performed under financial assistance award 70NANB24H134 from the National Institute of Standards and Technology, U.S. Department of Commerce.

## References

1 I. Nielsen, D. Dzodan, D. O. Ojwang, P. F. Henry, A. Ulander, G. Ek, L. Häggström, T. Ericsson, H. L. B. Boström and W. R. Brant, Water driven phase transitions in Prussian White cathode materials, *JPhys Energy*, 2022, **4**, 044012.
2 J. Hu, H. Tao, M. Chen, Z. Zhang, S. Cao, Y. Shen, K. Jiang and M. Zhou, Interstitial Water Improves Structural Stability of Iron Hexacyanoferrate for High-Performance Sodium-Ion Batteries, *ACS Appl. Mater. Interfaces*, 2022, **14**, 12234–12242.
3 I. Nielsen, A. Ulander, F. Juranyi, S. R. Larsen, M. Karlsson, W. R. Brant and M. S. Andersson, Impact of Sodium on the Water Dynamics in Prussian Blue Analogues, *Chem. Mater.*, 2024, **36**, 11246–11253.
4 A. Rudola, K. Du and P. Balaya, Monoclinic Sodium Iron Hexacyanoferrate Cathode and Non-Flammable Glyme-Based Electrolyte for Inexpensive Sodium-Ion Batteries, *J. Electrochem. Soc.*, 2017, **164**, A1098–A1109.
5 D. O. Ojwang, L. Häggström, T. Ericsson, R. Mogensen and W. R. Brant, Guest water hinders sodiumion diffusion in low-defect Berlin green cathode material, *Dalton Trans.*, 2022, **51**, 14712–14720.
6 D. A. Keen, Total scattering and the pair distribution function in crystallography, *Crystallogr. Rev.*, 2020, **26**, 141–199.
7 H. L. B. Boström and W. R. Brant, Octahedral tilting in Prussian blue analogues, *J. Mater. Chem. C*, 2022, **10**, 13690–13699.
8 I. Nielsen, C. A. Hall, A. M. Mattsson, R. Younesi, A. Buckel, G. Ek and W. R. Brant, Unravelling the origin of capacity fade in Prussian white hard carbon full cells through operando X-ray diffraction, *J. Mater. Chem. A*, 2024, **12**, 17413–17421.
9 J. Cattermull, B. Jagger, S. J. Cassidy, S. Dhir, P. K. Allan, M. Pasta and A. L. Goodwin, Non-equilibrium Ion Transport in a Hybrid Battery Material, arXiv, 2025, preprint, arXiv: 2509.04587, DOI: 10.48550/arXiv.2509.04587, 1–18.
10 J. Neuefeind, M. Feygenson, J. Carruth, R. Hoffmann and K. K. Chipley, The Nanoscale Ordered MAterials Diffractometer NOMAD at the Spallation Neutron Source SNS, *Nucl. Instrum. Methods Phys. Res., Sect. B*, 2012, **287**, 68–75.
11 A. A. Coelho, TOPAS and TOPAS-Academic: An optimization program integrating computer algebra and crystallographic

objects written in C++, *J. Appl. Crystallogr.*, 2018, **51**, 210–218.
12 C. L. Farrow, P. Juhas, J. W. Liu, D. Bryndin, E. S. Boin, J. Bloch, T. Proffen and S. J. Billinge, PDFfit2 and PDFgui: Computer programs for studying nanostructure in crystals, *J. Phys.: Condens. Matter*, 2007, **19**, 1–7.
13 M. G. Tucker, D. A. Keen, M. T. Dove, A. L. Goodwin and Q. Hui, RMC Profile: Reverse Monte Carlo for polycrystalline materials, *J. Phys.: Condens. Matter*, 2007, **19**, 1–16.
14 Y. Zhang, M. Eremenko, V. Krayzman, M. G. Tucker and I. Levin, New capabilities for enhancement of RMCProfile: Instrumental profiles with arbitrary peak shapes for structural refinements using the reverse Monte Carlo method, *J. Appl. Crystallogr.*, 2020, **53**, 1509–1518.
15 D. A. Keen, A comparison of various commonly used correlation functions for describing total scattering, *J. Appl. Crystallogr.*, 2001, **34**, 172–177.
16 Images and video generated using CrystalMaker®: a crystal and molecular structures program for Mac and Windows. CrystalMaker Software Ltd, Oxford, England. https://www.crystalmaker.com.
17 W. R. Brant, R. Mogensen, S. Colbin, D. O. Ojwang, S. Schmid, L. Häggström, T. Ericsson, A. Jaworski, A. J. Pell and R. Younesi, Selective Control of Composition in Prussian White for Enhanced Material Properties, *Chem. Mater.*, 2019, **31**, 7203–7211.
18 D. O. Ojwang, L. Häggström, T. Ericsson, J. Angström and W. R. Brant, Influence of sodium content on the thermal behavior of low vacancy Prussian white cathode material, *Dalton Trans.*, 2020, **49**, 3570–3579.
19 D. O. Ojwang, M. Svensson, C. Njel, R. Mogensen, A. S. Menon, T. Ericsson, L. Häggström, J. Maibach and W. R. Brant, Moisture-Driven Degradation Pathways in Prussian White Cathode Material for Sodium-Ion Batteries, *ACS Appl. Mater. Interfaces*, 2021, **13**, 10054–10063.
20 H. M. Rietveld, A profile refinement method for nuclear and magnetic structures, *J. Appl. Crystallogr.*, 1969, **2**, 65–71.
21 J. Barthel, Dr Probe: a software for high-resolution STEM image simulation, *Ultramicroscopy*, 2018, **193**, 1–11.
22 K. Sada, D. J. Siegel, A. Manthiram and D. Ph, Unveiling the Influence of Water Molecules on the Structural Dynamics of Prussian Blue Analogues, *Angew. Chemie*, 2024, **2406853**, 1–11.
23 N. Tapia-Ruiz, *et al.*, 2021 Roadmap for Sodium-Ion Batteries, *JPhys Energy*, 2021, **3**, 031503.
24 V. Krayzman, I. Levin, J. C. Woicik, T. Proffen, T. A. Vanderah and M. G. Tucker, A combined fit of total scattering and extended X-ray absorption fine structure data for local-structure determination in crystalline materials, *J. Appl. Crystallogr.*, 2009, **42**, 867–877.
25 D. Boras, I. Nielsen, A. Buckel, T. Ericsson, L. Häggström, R. Younesi, T. Stabb and W. R. Brant, Determening internal porosity in Prussian blue analogue cathode materials using poistron annihilation lifetime spectroscopy, *J. Mater. Sci.*, 2023, **58**, 16344–16356.
26 J. Song, L. Wang, Y. Lu, J. Liu, B. Guo, P. Xiao, J. J. Lee, X. Q. Yang, G. Henkelman and J. B. Goodenough, Removal of Interstitial $H_2O$ in Hexacyanometallates for a Superior Cathode of a Sodium-Ion Battery, *J. Am. Chem. Soc.*, 2015, **137**, 2658–2664.
27 C. Ling, J. Chen and F. Mizuno, First-principles study of alkali and alkaline earth ion intercalation in iron hexacyanoferrate: the important role of ionic radius, *J. Phys. Chem. C*, 2013, **117**, 21158–21165.
28 S. Liu and K. C. Smith, Effects of interstitial water and alkali cations on the expansion, intercalation potential, and orbital coupling of nickel hexacyanoferrate from first principles, *J. Appl. Phys.*, 2022, **131**, 105101.
29 P. Xiao, J. Song, L. Wang, J. B. Goodenough and G. Henkelman, Theoretical study of the structural evolution of a $Na_2FeMn(CN)_6$ Cathode upon Na Intercalation, *Chem. Mater.*, 2015, **27**, 3763–3768.
30 F. S. Hegner, J. R. Galán-Mascarós and N. López, A Database of the Structural and Electronic Properties of Prussian Blue, Prussian White, and Berlin Green Compounds through Density Functional Theory, *Inorg. Chem.*, 2016, **55**, 12851–12862.
31 L. Deng, J. Qu, X. Niu, J. Liu, J. Zhang, Y. Hong, M. Feng, J. Wang, M. Hu, L. Zeng, Q. Zhang, L. Guo and Y. Zhu, Defect-free potassium manganese hexacyanoferrate cathode material for high-performance potassiumion batteries, *Nat. Commun.*, 2021, **12**, 1–9.
32 J. Cattermull, M. Pasta and A. L. Goodwin, Structural complexity in Prussian blue analogues, *Mater. Horiz.*, 2021, **8**, 3178–3186.
33 I. Nielsen, Y. Cheng, F. Schwarz, A. Mace, H. Cavaye, J. Armstrong, M. G. Tucker, M. Karlsson, W. R. Brant and M. S. Andersson, Vibrational water dynamics in sodium-based Prussian blue analogues. Under revision in, *J. Phys. Chem. C*, 2025, DOI: 10.1021/acs.jpcc.5c05783.
34 F. M. Maddar, D. Walker, T. W. Chamberlain, J. Compton, A. S. Menon, M. Copley and I. Hasa, Understanding dehydration of Prussian White: from material to aqueous processed composite electrodes for sodium-ion battery application, *J. Mater. Chem. A*, 2023, **11**, 15778–15791.
35 A. Clavelin, D. L. Thanh, I. Bobrikov, M. Fehse, N. E. Drewett, A. L. Gabriel, D. Saurel and M. Galceran, Dehydration Conditions and Ultrafast Rehydration of Prussian White: Phase Transition Dynamics and Implications for Sodium-Ion Batteries. ACS, *Mater. Lett.*, 2024, **6**, 5208–5214.

 